

Machine Learning Classifies Ferroptosis and Apoptosis Cell Death Modalities with TfR1 Immunostaining

Jenny Jin,[▽] Kenji Schorpp,[▽] Daniel Samaga,[▽] Kristian Unger, Kamyar Hadian,* and Brent R. Stockwell*



Cite This: <https://doi.org/10.1021/acscchembio.1c00953>



Read Online

ACCESS |



Metrics & More



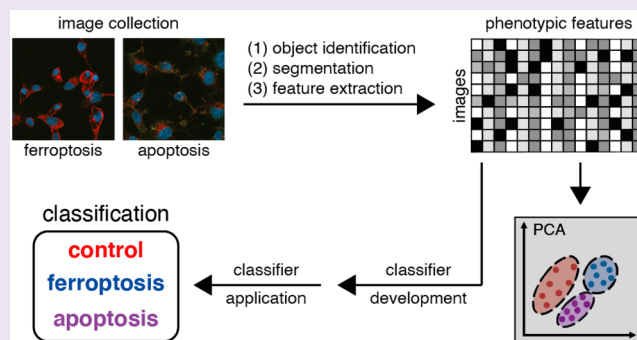
Article Recommendations



Supporting Information

ABSTRACT: Determining cell death mechanisms occurring in patient and animal tissues is a longstanding goal that requires suitable biomarkers and accurate quantification. However, effective methods remain elusive. To develop more powerful and unbiased analytic frameworks, we developed a machine learning approach for automated cell death classification. Image sets were collected of HT-1080 fibrosarcoma cells undergoing ferroptosis or apoptosis and stained with an antitransferrin receptor 1 (TfR1) antibody, together with nuclear and F-actin staining. Features were extracted using high-content-analysis software, and a classifier was constructed by fitting a multinomial logistic lasso regression model to the data. The prediction accuracy of the classifier within three classes (control, ferroptosis, apoptosis) was 93%. Thus, TfR1

staining, combined with nuclear and F-actin staining, can reliably detect both apoptotic and ferroptosis cells when cell features are analyzed in an unbiased manner using machine learning, providing a method for unbiased analysis of modes of cell death.



INTRODUCTION

Regulated cell death is a complex and tightly regulated phenomenon, involving intricate molecular mechanisms. For numerous cell death processes, molecular markers have been developed that identify cells undergoing apoptosis¹ or necroptosis² through immunolabeling. Such markers may be used in cell culture and tissue histopathological applications to examine the prevalence of cell death processes, which may improve the treatment and diagnosis of diseases in which these processes are implicated.

Ferroptosis is a form of regulated cell death characterized by the iron-dependent accumulation of lipid peroxides, as well as the loss of cellular antioxidant repair capabilities.³ The enzyme glutathione peroxidase 4 (GPX4) is a cellular regulator of lipid peroxidation levels, and several ferroptosis inducers have been developed that specifically target the activity of this enzyme through direct inhibition (e.g., RSL3).⁴ A second class of ferroptosis inducers (e.g., IKE and erastin) causes inactivation of GPX4 through depletion of glutathione via inhibition of the antiporter system x_c^- .⁵ Ferroptosis has been implicated in several disease pathologies, such as degenerative diseases and organ injury.^{6,7} Furthermore, ferroptosis induction may have potential as a cancer treatment strategy.^{8,9}

Toward the goal of specific identification of ferroptosis in tissue samples, we previously discovered an effective ferroptosis-staining reagent, 3F3 anti-Ferroptotic Membrane Antibody (3F3-FMA), that can be used to stain cells and tissue samples directly.¹⁰ The antigenic target of 3F3-FMA is transferrin receptor 1 (TfR1), a membrane receptor that

internalizes iron-bound transferrin through receptor-mediated endocytosis.¹¹ This iron uptake activity of TfR1 contributes to intracellular iron levels necessary for ferroptosis.¹² 3F3-FMA, as well as other anti-TfR1 antibodies, exhibit an increase in total and membrane-localized fluorescence when used to stain cells undergoing ferroptosis in culture (compared to vehicle-treated control cells). TfR1 has been used to identify the occurrence of ferroptosis in traumatic brain injury¹³ and myocardial ischemia/reperfusion injury,¹⁴ among other uses. Thus, TfR1 serves as a biomarker to facilitate the identification of ferroptosis in cell and tissue contexts.

The identification of plasma membrane fluorescence as a distinguishing feature between ferroptosis and other cell death processes upon staining with anti-TfR1 antibodies was discovered using visual inspection; here, we sought instead to evaluate the use of machine learning as an unbiased tool to detect ferroptotic cells. Machine learning methods facilitate the high-throughput analysis of cell image sets versus tedious and subjective manual processes; in cell biology applications, machine learning can increase processing capabilities and objectivity. The supervised machine learning pipeline involves

Received: December 4, 2021

Accepted: February 22, 2022

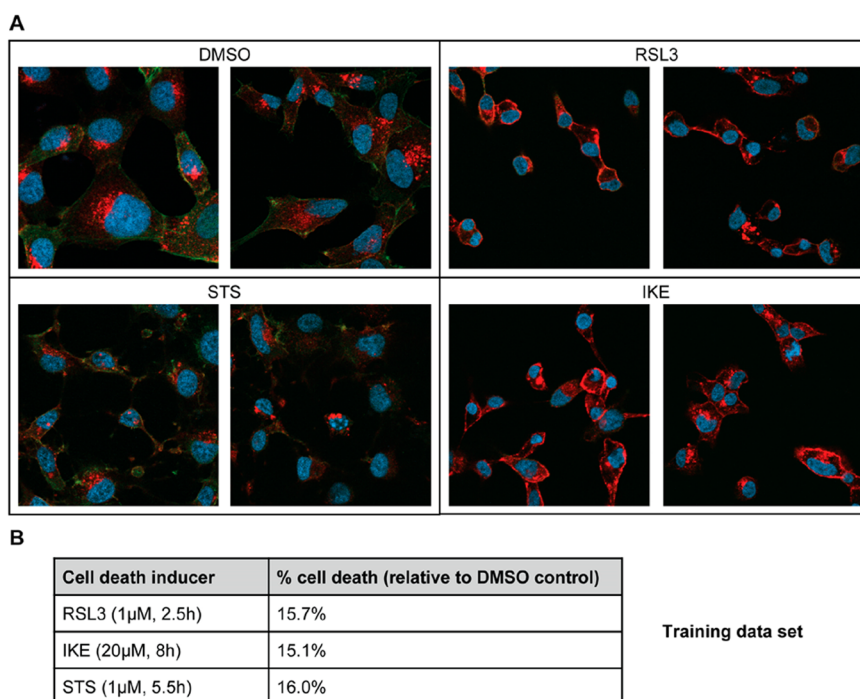


Figure 1. Images undergoing different cell death modalities for machine learning analysis. (A) HT-1080 cells were incubated with ferroptosis inducers RSL3 (1 μ M) or IKE (20 μ M), apoptosis inducer STS (1 μ M), or DMSO control. Nuclei were stained with DAPI (blue). Tfr1 was labeled with 3F3-FMA and Alexa Fluor 594 secondary antibody (red). F-actin was labeled with FITC-phalloidin (green). Images were captured using a Zeiss LSM800 confocal microscope at 63 \times /1.40 oil DIC objective. For each treatment, representative images from the training data set are depicted. (B) In parallel with the immunofluorescence experiments, CellTiter-Glo viability assays were used to monitor the percentage cell death for each treatment, and cells were fixed when percentage cell death reached 10–20%. The concentrations and time points that resulted in this extent of cell death in each set are listed for each treatment.

69 image collection and preprocessing, object detection, and
 70 feature extraction and prioritization.¹⁵ Our goals were to assess
 71 the machine learning potential in discriminating ferroptosis,
 72 apoptosis, and control-treated samples as well as to provide a
 73 pipeline for identification of features that best distinguish those
 74 cell death modalities in our setting.

75 Therefore, after collecting images of fluorescently stained
 76 cells treated with vehicle only or undergoing ferroptosis or
 77 apoptosis, images were analyzed via high-content-image
 78 analysis, and a classifier was trained on the extracted data.
 79 The trained classifier corresponds to a nonexclusive list of
 80 informative features with assigned coefficients, which was
 81 validated with a second data set by successfully predicting the
 82 same classes. These results expand and strengthen the
 83 applicability of biomarkers, such as 3F3-FMA/Tfr1, for
 84 differentiating cell death mechanisms in an objective and
 85 high-throughput manner.

86 ■ RESULTS AND DISCUSSION

87 To explore the application of machine learning to the
 88 classification of different cell death modalities, we collected
 89 large numbers of images of cells fixed and immunofluor-
 90 escently stained with 3F3 anti-Ferroptotic Membrane Anti-
 91 body (3F3-FMA), a ferroptosis-specific antibody with Tfr1 as
 92 its target antigen. Specifically, HT-1080 cells were treated with
 93 ferroptosis inducers (RSL3, a GPX4 inhibitor, or IKE, a system
 94 x_c^- inhibitor), an apoptosis inducer (staurosporine, STS),¹⁶ or
 95 DMSO vehicle control. In addition to being stained with anti-
 96 Tfr1 3F3-FMA (labeled with AlexaFluor 594), cells were
 97 stained with DAPI as a nuclear marker and FITC-phalloidin as

a cytoplasmic (F-actin) marker to assist identification of 98
 cellular features for machine learning classification (see below). 99

Machine learning tools are designed to adapt to any data 100
 pattern associated with the task to learn. There were several 101
 important aspects to consider in collecting images for machine 102
 learning classification. First, all treatments within a day (i.e., 103
 using the same microscope settings) were balanced. Moreover, 104
 we collected all images of the discovery data on day 1 and the 105
 validation data later on a different day. Second, the extent of 106
 cell death was standardized across different conditions to 107
 analyze cells in an early stage of cell death induction. 108
 Specifically, we fixed cells under each treatment condition 109
 when they reached 10–20% cell death, so that cell death had 110
 been initiated, but not to the extent of excessive end-stage 111
 necrosis. At this point, the cells should still have intact cell 112
 membrane integrity and not have detached from the surface. 113
 The CellTiter-Glo (CTG) viability assay, which measures 114
 intracellular ATP levels as an indicator of viability, was used to 115
 monitor the extent of cell death. We performed a pilot study 116
 and established optimal concentration and time point ranges 117
 for each treatment (Figure S1). 118

Guided by the results of the pilot study, the first image set 119
 for training and discovery of classifiers was collected, and 120
 immunofluorescence experiments were performed when the 121
 extent of cell death reached 10–20% compared to DMSO 122
 control treatment in parallel CTG assays (Figure 1). Viewing 123
 the images, the characteristic membrane localization of the 124
 3F3-FMA signal can be seen in ferroptotic cells compared to 125
 the DMSO control,¹⁰ and characteristic membrane blebbing 126
 can be observed in apoptotic cells.¹⁷ 127

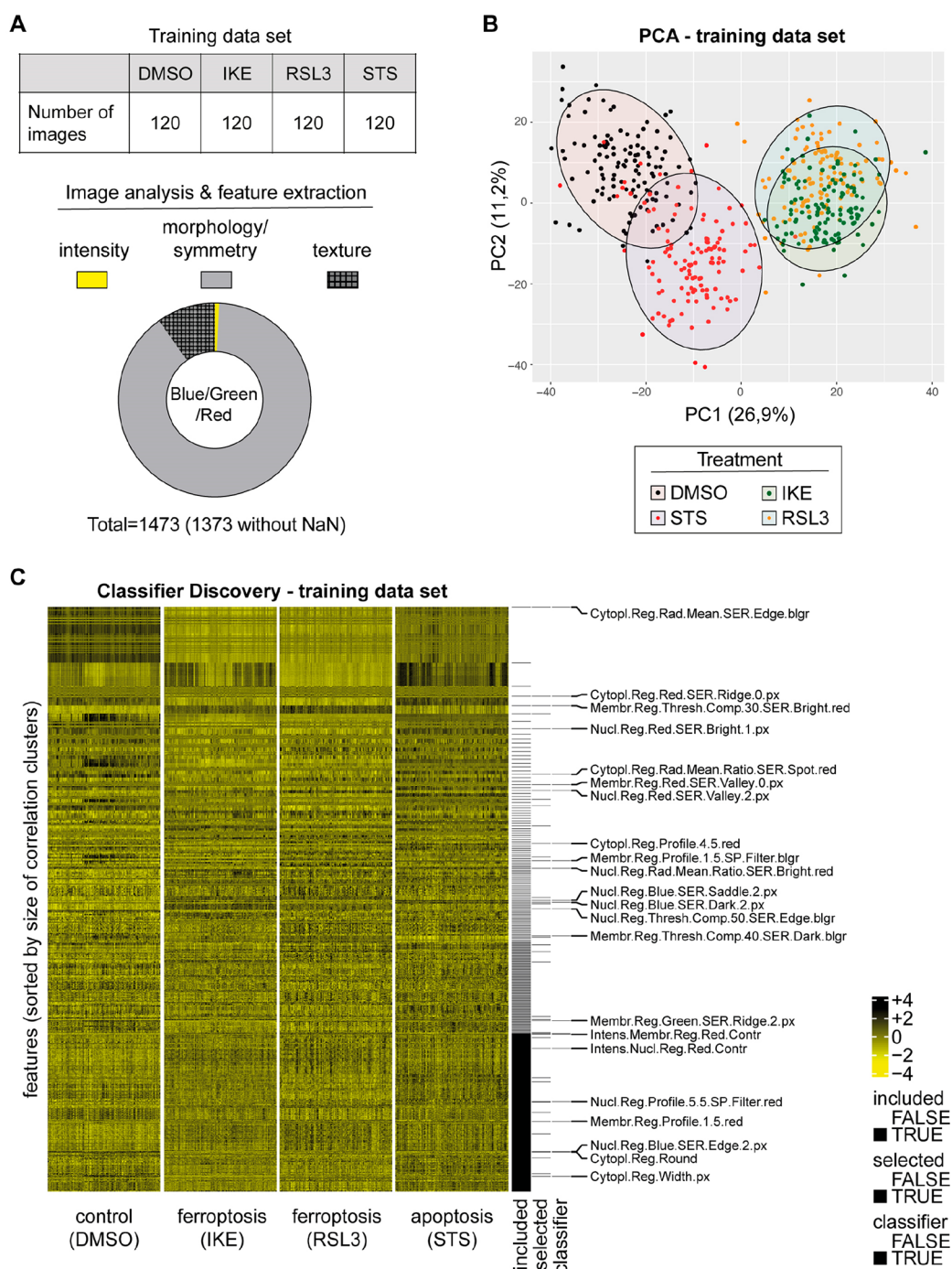


Figure 2. Feature extraction and classifier discovery. (A) The experiment consisted of 120 images per condition (DMSO, IKE, RSL3, STS). The image analysis software extracted 1473 features for the blue, green, and red fluorescence signals. The features can roughly be grouped in intensity, morphology/symmetry, and texture features. Undefined values (NaN, “Not a Number”). (B) Principal component analysis of 1373 features extracted from the images. Individual images are visualized as points on the scatter plot of the first two principal components. The color code is according to the treatment label (red = DMSO, blue = RSL3, green = IKE, and purple = STS) and was added after the PCA was conducted. (C) Feature matrix of the training data set (scaled for visualization purposes) is cleared for highly correlated features (“included”) and informative features are isolated by pairwise logistic lasso regressions (“selected”). Finally, a multinomial logistic lasso regression model is fitted to the reduced feature matrix, and a classifier is identified (“classifier”: 23 features with corresponding regression model coefficients). blgr = bluegreen

128 For the training set, once the cells were fixed and stained
 129 with DAPI, FITC-phalloidin, and anti-TfR1 3F3-FMA, 120
 130 images were collected per treatment condition (DMSO
 131 control, RSL3, IKE, STS) with an average of 10 cells per
 132 image (Figure 2A), which corresponds to a cell density of
 133 approximately 80% for DMSO-treated cells. Subsequently, we

analyzed images with the PerkinElmer Columbus high-
 content-analysis software. For this purpose, nuclei were
 identified using the DAPI signal, and based on this, the
 cytoplasm and the membrane regions were segmented using
 the F-actin signal (Figure S2). The intensity, the
 and the symmetry of the objects, as well as the texture and

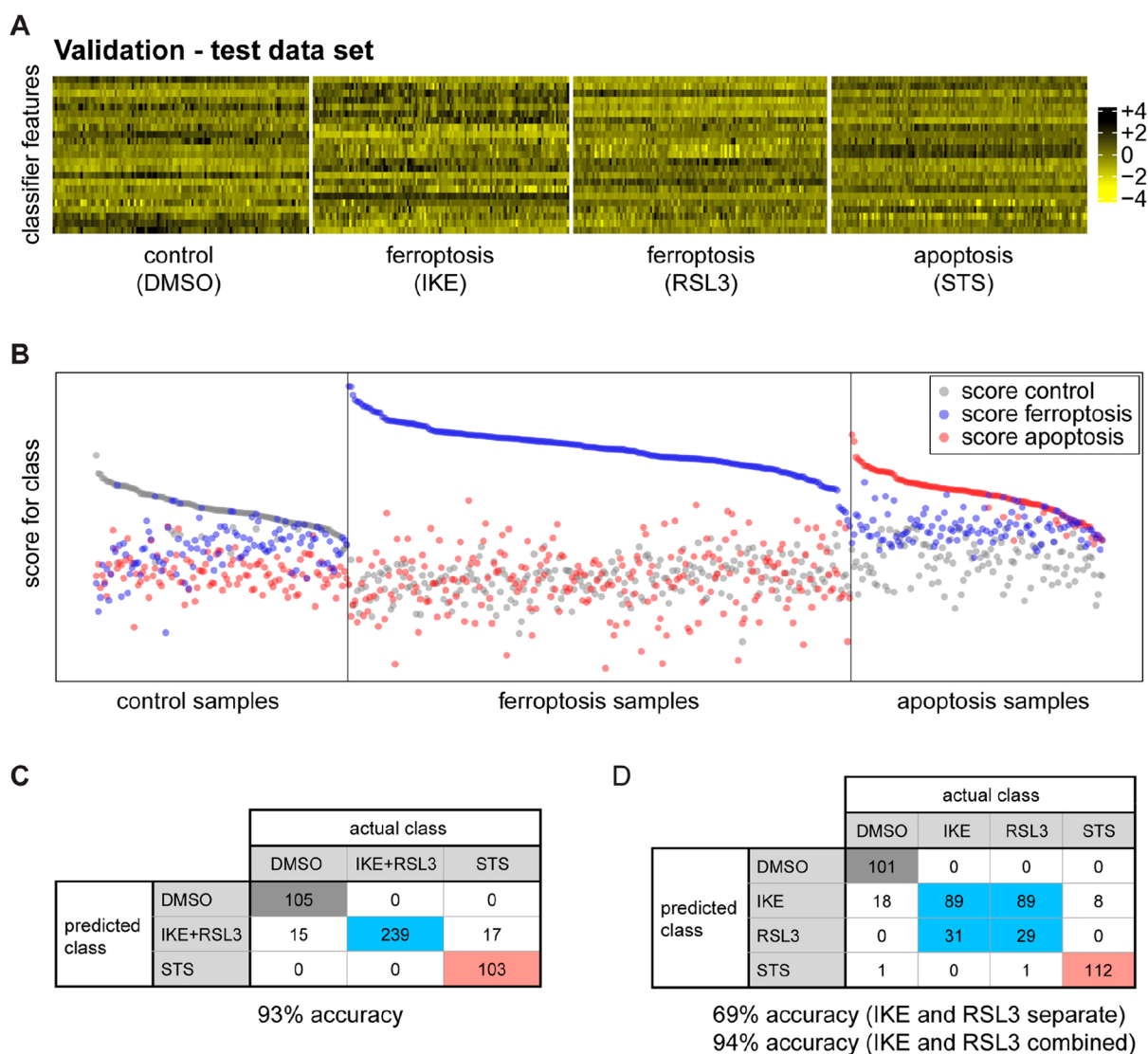


Figure 3. Model validation. (A) The classifier was applied to the independent test data set for model validation. (B) Comparison of the known class with the predicted class measures classifier performance. Each class is enriched in the corresponding samples, thereby validating the model. (C and D) Confusion tables for the multiclass prediction. (C) DMSO, IKE+RSL3, and STS classes are predicted with an accuracy of 93%. (D) DMSO, IKE, RSL3, and STS are predicted with 94% accuracy, when IKE and RSL3 are combined.

140 structure of the fluorescence signal, were determined within
 141 these cell segments for the blue, green, and red channels,
 142 respectively. Consequently, we were able to extract a large
 143 number of features for each image. Importantly, during the
 144 analysis, the features for single cells were averaged for each
 145 image (median). This gave rise to 120 observations per
 146 treatment for each feature. The blue (DAPI) and green (FITC-
 147 phalloidin) channel provided together 738 features, while the
 148 red (TfR1) channel provided 735 features (Figure S2). Among
 149 these features, there were frequently used features such as
 150 “Number of Nuclei”, “Nucleus Intensity”, and “Nucleus
 151 Roundness”. As expected, different effects are visible for
 152 basic features after treatment, but no reasonable classification
 153 could be made (Figure S3A–C). In order to validate the
 154 quality of the data, we analyzed the membrane fluorescence
 155 intensity for the TfR1 signal. As expected, we found a
 156 significant increase in TfR1 fluorescence intensity after
 157 treatment with RSL3 and IKE but not upon treatment with
 158 DMSO or STS (Figure S3D).

We then removed all features that contained undefined 159
 values (NaN, “Not a-Number”) and reduced the number of 160
 features from 1473 to 1,373. We performed a principal 161
 component analysis (PCA) with the data matrix of 1373 162
 features and a total of 480 observations (= 120 images per 163
 condition; DMSO, IKE, RSL3, and STS) and visualized 164
 principal components 1 and 2 (Figure 2B). The cells treated 165
 with RSL3 and IKE separated well from the other samples in 166
 the first principal component (Figure 2B). As expected, the 167
 RSL3-treated and IKE-treated samples overlapped in the first 168
 two principal components, as both induce the same type of cell 169
 death modality, namely ferroptosis. Cells treated with STS also 170
 separated from the DMSO population, although to a lesser 171
 extent compared to ferroptosis inducers. STS differs not only 172
 from the vehicle DMSO but also from RSL3 and IKE, although 173
 cell death in the CTG viability assay performed in parallel was 174
 almost identical. This indicated that the staining and analysis 175
 strategy was able to distinguish vehicle-treated from 176
 ferroptosis, and from apoptosis. 177

178 This data set was then used for supervised machine learning
179 to build a classifier that would allow the determination of
180 whether treatments of cells with certain substances trigger
181 ferroptosis or apoptosis (Figure 2C).

182 A classifier is a mathematical function or procedure that
183 assigns a sample to one or several classes, usually by calculating
184 class scores for each sample (i.e., image) from its feature
185 values. With respect to the type of mathematical procedure,
186 classifiers vary in terms of interpretability and transferability to
187 new data sets. Multinomial logistic regression models using the
188 lasso (least absolute shrinkage and selection operator)
189 inherently provide a feature selection and return a vector of
190 coefficients for the selected features, called signature, which is
191 directly interpretable and transferable.

192 For numerical stability of a treatment classifier, all non-
193 normally distributed features (Shapiro–Wilk test of normality
194 in discovery data, $\alpha = 0.05$) were Box-Cox transformed
195 (parameters $\lambda_1 = 0$ and $\lambda_2 = 1$ if the p value of this
196 test was increased by transformation). Reduction of
197 dimensionality was carried out by removal of redundancies
198 (according to feature-pairwise Pearson correlation of $|r| > 0.9$
199 in discovery data) and by preselection of informative features
200 through treatment-pairwise logistic lasso regression analysis.
201 Notably, only informative features of limited correlation
202 among each other were used for signature discovery. The
203 CRAN package `glmnet` was used to perform multinomial
204 logistic lasso regression.¹⁹ For classification of three groups
205 (DMSO; IKE/RSL3; STS), a signature of 23 features was
206 identified (Table S1). These features have biological meanings
207 and can be interpreted as such: for instance, the feature
208 “Membrane.Region.Red.SER.Valley.0.px” is based on texture
209 changes (= SER.Valley.0.px; SER = Spots, Edges and Ridges)
210 of the TfR1 staining (= Red) within the cell membrane (=
211 Membrane.Region). We have previously shown that TfR1
212 plasma membrane intensity staining changes under ferroptotic
213 conditions.¹⁰ Thus, it is plausible that this feature should be
214 represented in a classifier signature. Interestingly, the signature
215 also consists of features that are not TfR1 related. For example,
216 the feature “Nucleus.Region.Blue.SER.Saddle.2.px” describes a
217 texture (SER.Saddle.2.px) in the nucleus that is determined
218 using the blue channel (DNA staining). Importantly, this
219 particular texture changes upon treatment with apoptosis
220 inducers, which is expected as apoptosis induces alterations to
221 DNA and chromatin structure. Similar to these two examples,
222 the biological context of features can be interpreted.

223 Together, this unbiased approach to classifier identification
224 offers the possibility of discovering features that previously
225 have not been considered in cell death. Hence, this strategy
226 allows the development of a signature using features whose
227 changes human eyes would not necessarily perceive and helps
228 to more accurately classify cell death states. Notably, there are
229 highly correlated features in the full data set (Table S2), which
230 are potentially replaceable in the classifier (after refitting the
231 coefficients). Features that were not included in the classifier
232 are not necessarily uninformative—they were not selected,
233 because they do not contribute additional information to
234 improve the classifier.

235 We then collected an independent second image set—using
236 the same conditions with viabilities in the 80–90% range
237 (Figure S4A)—in order to generate biological replicates for
238 model validation (Figure S4B). For this experiment, termed
239 the “validation experiment”, we ran an identical analysis to
240 extract image data and generated the same set of features as

was used in the “training experiment”. For model validation, 241
the data from the validation experiment was used to challenge 242
the identified classifier. The coefficients of the 23 features in 243
the classifier were used to predict the class of the samples in 244
the validation experiment, i.e., control, ferroptosis, or apoptosis 245
(Figure 3A,B). The accuracy of prediction for the three classes 246
of control (DMSO), ferroptosis (RSL3+IKE), or apoptosis 247
(STS) was 93% (447 out of 479 cases correct; Figure 3C). 248

A four-class classifier trained to distinguish the three 249
inducers (IKE, RSL3, and STS), as well as the DMSO control, 250
did not differentiate between IKE and RSL3, as expected. Both 251
classes were assigned identically to IKE (89 cases each) or 252
RSL3 (31 and 29 cases) and minimally to STS (0 or 1 case). 253
Combining IKE and RSL3 resulted in an accuracy of 94% 254
(Figure 3D). Consistently, even when excluded from model 255
discovery, IKE validation set images were constantly identified 256
as RSL3-like by two-class logistic lasso regression classifiers 257
trained to discriminate DMSO control from RSL3 or STS from 258
RSL3 (120 of 120 and 113 of 120 images, respectively—see 259
supplementary PDF file “MachineLearning_Ferroptosis_ 260
SI.pdf”: “Binary Prediction”). Importantly, this suggests that 261
both ferroptosis inducers induce a similar phenomenology with 262
respect to the features extracted from the images. 263

The classifier performed well for detecting ferroptosis, as 264
TfR1 is a known ferroptosis marker, and features from this 265
channel are prominently represented in the signature. 266
However, we were intrigued that apoptosis was also readily 267
distinguished from the control group using the developed 268
signature. 269

This classifier is based on images of cells treated with 270
ferroptosis or apoptosis inducers and stained with anti-TfR1 271
3F3-FMA, DAPI, and FITC-Phalloidin. It is important to 272
consider that for any new (unknown) small molecule that is 273
desired to be tested with this classifier, the concentration and 274
incubation times reducing the viability to 80–90% have to be 275
identified in advance. Standardized microscopy image acquis- 276
ition of treated cells in combination with this classifier could 277
provide the information on whether the substances induce 278
ferroptosis or apoptosis. As with any analysis tool, some 279
refinement might be needed. 280

Further, this work may have important implications for 281
tissue analysis and allow for a high-throughput, objective 282
procedure to identify ferroptosis and other cell death 283
modalities in a tissue context, whether with animal disease 284
models or patient samples. One such application may involve 285
assessing the response of cancer patients to therapy. 286

This classifier cannot directly be applied to images taken 287
under entirely different conditions (treatments, staining, etc.). 288
However, we present a workflow on how researchers can 289
develop a classifier based on a training image set for various 290
cell death processes with the help of standardization of 291
experiments and corresponding analysis tools. Hence, this 292
strategy may serve as a blueprint to be employed for the 293
detection of other cell death pathways, including necroptosis 294
and pyroptosis, and ultimately a universal classifier that detects 295
and classifies all of the major types of cell death. 296

297 METHODS

Cell Culture. HT-1080 (ATCC Cat# CRL-7951, RRID:CVCL 298
0317) cells were grown in Dulbecco’s Modified Eagle Medium 299
(DMEM) with 10% fetal bovine serum, 1% penicillin-streptomycin, 300
and 1% nonessential amino acids. Cells were grown in a humidified 301
incubator at 37 °C and 5% CO₂. 302

303 **CellTiter-Glo Assay.** HT-1080 cells were plated in technical
304 triplicates in white opaque 96-well plates at 15 000 cells/100 μL
305 media per well. For the pilot experiment, the cells were treated with 1
306 μM RSL3, 20 μM IKE, or 1 μM staurosporine (STS) at different time
307 points. For the immunofluorescence experiments, the cells were
308 treated at the time points determined in the pilot experiment and
309 several time points before and after. A total of 100 μL of 50%
310 CellTiter-Glo (Promega) and 50% cell culture medium was added to
311 each well, and the cells were incubated and shaken for 2 min at RT.
312 Luminescence was measured using a Victor X5 plate reader
313 (PerkinElmer).

314 **Immunofluorescence (IF).** HT-1080 cells were treated with 1
315 μM RSL3, 20 μM IKE, or 1 μM STS on poly lysine-coated coverslips
316 (Sigma-Aldrich P4832) in 24-well plates. When the cell death
317 percentage reached around 10–20% (determined using the CellTiter-
318 Glo assay), media were removed, and the cells were gently washed
319 with PBS²⁺ (PBS with 1 mM CaCl₂ and 0.5 mM MgCl₂) twice,
320 ensuring the cells did not dry out. The cells were fixed and
321 permeabilized with 4% PFA in PBS with 0.1% Triton X-100 (PBT),
322 with 200 μL per well. The plates were covered with foil, and the cells
323 were incubated and shaken at RT for 15–20 min. The PFA was
324 disposed of safely, and the cells were washed with PBT three times.
325 The cells were blocked with 5% normal goat serum (NGS;
326 ThermoFisher 50197Z) in PBT for 1 h at RT. The cells were then
327 incubated with mouse 3F3 anti-Ferroptotic Membrane Antibody
328 (3F3-FMA) at a 1:500 dilution in PBT with 1% bovine serum
329 albumin (BSA) and 5% NGS at 4 °C overnight. The cells were
330 washed with PBT for 5 min three times. The cells were then
331 incubated with goat antimouse IgG (H+L) Highly Cross-Adsorbed
332 Secondary Antibody, Alexa Fluor 594 (Thermo Fisher Scientific Cat#
333 A-11032, RRID:AB_2534091) at 1:200 dilution, and FITC-phalloidin
334 at 1:1000 dilution in PBT with 1% BSA for 1 h at RT. The cells were
335 washed with PBT for 5 min three times. The cells were placed on
336 slides using Prolong Diamond antifade mountant with DAPI
337 (ThermoFisher P36962). All images were collected on a Zeiss LSM
338 800 confocal microscope using a Plan-Apochromat 63 \times /1.40 oil DIC
339 objective with constant laser intensity for all images.

340 **Automated Image Analysis.** Image analysis was performed
341 using Columbus software version 2.8.0 (PerkinElmer). In the
342 following, the analysis steps in Columbus are described: the DAPI
343 and FITC signals were smoothed for the cell segmentation process
344 using Median filters to reduce noise signals. Nuclei were detected via
345 the DAPI signal. The FITC channel was used to define the cytoplasm
346 and membrane region. In a next step, morphology/symmetry features,
347 texture (SER features), and intensity properties of the DAPI, FITC,
348 and red channel were calculated for each cell region (nuclei,
349 cytoplasm, and membrane). Moreover, we applied a filter to remove
350 border objects (nuclei that cross image borders). For the detailed
351 analysis pipeline in Columbus, please see Figure S2 and the analysis
352 sequences.

353 **Statistical Data Analysis: Transformation and Feature
354 Selection.** From two data sets containing 480 samples each (120
355 DMSO, 120 IKE, 120 RSL3, 120 STS) 1473 features were generated
356 and exported by the Columbus imaging software. The data sets were
357 filtered for completeness, i.e., all features containing “not-a-number”
358 (NaN) were excluded from analysis, resulting in 1373 features. The
359 data set generated first was assigned to model discovery, the second
360 data set to model validation. Features that were non-normally
361 distributed in the discovery data according to the Shapiro test for
362 normality ($p < 0.05$) were log-transformed (i.e., $\log(1 + x)$) also
363 known as two-parameter Box–Cox transformation with $\lambda_1 = 0$
364 and $\lambda_2 = 1$), if the transformed data were closer to normality in
365 terms of the Shapiro-test p value. Of all pairs of features that were
366 highly correlated in the discovery data (i.e., absolute Pearson
367 correlation coefficient of larger than 0.9), one member was excluded
368 from analysis iteratively; starting with the feature participating in the
369 largest number of correlations in the training data set for classifier
370 discovery, which was preserved, all highly correlated features were
371 removed from both data sets.

Classifier Discovery. Further feature preselection was conducted
372 on the discovery data by logistic regression for pairwise classification
373 among control, ferroptosis, and apoptosis using the lasso (least
374 absolute shrinkage and selection operator).¹⁸ All features that were
375 selected at least once in the pairwise logistic regressions were
376 preserved in the training data set for classifier discovery, on which the
377 classifier was trained. For classification, a multinomial logistic
378 regression model with the lasso was used, resulting in a signature
379 for sample classification. Lambda.1se was used as a criterion for
380 selection of the optimal penalty parameter. The quality of this
381 signature was determined in terms of accuracy of classification of the
382 validation data, where true class membership is known. The
383 importance of signature features was estimated by the product of
384 the standard deviation of the transformed feature in the discovery data
385 and the coefficient in the regression model. All statistical calculations
386 were conducted using R version 4.0.3; for lasso regression, the glmnet
387 package was used.¹⁹ 388

Data Availability Statement. The data underlying this study
389 (raw data as txt files, R code Rmd file, and complete and intermediate
390 Rdata files) are openly available in Columbia University Academic
391 Commons at 10.7916/3hdp-9j07. 392

■ ASSOCIATED CONTENT

 393

Supporting Information

 394

The Supporting Information is available free of charge at
395 <https://pubs.acs.org/doi/10.1021/acscchembio.1c00953>. 396

Description of concepts, data transformation, binary
397 prediction as proof of principle, multiclass prediction
398 using multinomial logistic regression lasso model (PDF) 399
Pilot study results using CellTiter-Glo viability assay to
400 determine optimal cell death treatment concentration
401 and time point, workflow of automated image analysis,
402 segmentation, and feature extraction, boxplots of
403 representative features, viability data and principal
404 component analysis of validation experiment, analysis
405 sequences (Figures S1–S4) (PDF) 406
Signature of features in cell death classification (Table
407 S1) (XLSX) 408
List of features highly correlated to features in signature
409 (Table S2) (XLSX) 410

■ AUTHOR INFORMATION

 411

Corresponding Authors

 412

Brent R. Stockwell – Department of Biological Sciences,
413 Columbia University, New York, New York 10027, United
414 States; Department of Chemistry and Irving Institute for
415 Cancer Dynamics, Columbia University, New York, New
416 York 10027, United States; Herbert Irving Comprehensive
417 Cancer Center, Columbia University Irving Medical Center,
418 New York, New York 10032, United States; orcid.org/0000-0002-3532-3868; Email: bstockwell@columbia.edu 419

Kamyar Hadian – HelmholtzZentrum München, German
421 Research Center for Environmental Health, Cell Signaling
422 and Chemical Biology, Institute for Molecular Toxicology and
423 Pharmacology, 85764 Neuherberg, Germany; orcid.org/0000-0001-8727-2575; Email: kamyar.hadian@helmholtz-muenchen.de 424–426

Authors

 427

Jenny Jin – Department of Biological Sciences, Columbia
428 University, New York, New York 10027, United States;
429 Department of Chemistry, Columbia University, New York,
430 New York 10027, United States 431

Kenji Schorpp – HelmholtzZentrum München, German
432 Research Center for Environmental Health, Cell Signaling 433

434 and Chemical Biology, Institute for Molecular Toxicology and
435 Pharmacology, 85764 Neuherberg, Germany
436 Daniel Samaga – HelmholtzZentrum München, German
437 Research Center for Environmental Health, Research Unit
438 Radiation Cytogenetics, 85764 Neuherberg, Germany
439 Kristian Unger – HelmholtzZentrum München, German
440 Research Center for Environmental Health, Research Unit
441 Radiation Cytogenetics, 85764 Neuherberg, Germany

442 Complete contact information is available at:

443 <https://pubs.acs.org/10.1021/acscchembio.1c00953>

444 Author Contributions

445 [∇]These authors contributed equally

446 Author Contributions

447 J.J., K.S., K.H., and B.R.S. conceptualized experiments. J.J.
448 performed imaging collection and viability assays. K.S.
449 performed image analysis, feature extraction, and PCA. D.S.
450 and K.U. formulated the machine learning model and
451 performed classification. J.J., K.S., D.S., K.U., K.H., and
452 B.R.S. performed data analysis. All authors contributed to the
453 writing and editing of the manuscript.

454 Notes

455 The authors declare the following competing financial
456 interest(s): B.R.S. is an inventor on patents and patent
457 applications involving small molecule drug discovery, ferroptosis,
458 and 3F3-FMA; cofounded and serves as a consultant to
459 Inzen Therapeutics, Nevrox Limited, Exarta Therapeutics, and
460 ProjenX Inc.; and serves as a consultant to Weatherwax
461 Biotechnologies Corporation and Akin Gump Strauss Hauer &
462 Feld LLP. All other authors declare no competing financial
463 interest.

464 ■ ACKNOWLEDGMENTS

465 B.R.S. is supported by NCI grants P01CA87497 and
466 R35CA209896, National Institute of Neurological Disorders
467 and Stroke (NINDS) grants R61NS109407 and
468 R33NS109407, and NIH grant UG3CA256962. J.J. was
469 supported by the Columbia College Science Scholars program.

470 ■ REFERENCES

471 (1) Denton, D.; Kumar, S. Immunostaining Using an Antibody
472 against Active Caspase-3 to Detect Apoptotic Cells in *Drosophila*.
473 *Cold Spring Harb Protoc* **2015**, *2015*, 576–579.
474 (2) He, P.; Ai, T.; Yang, Z.-H.; Wu, J.; Han, J. Detection of
475 necroptosis by phospho-MLKL immunohistochemical labeling. *STAR*
476 *Protoc.* **2021**, *2*, 100251.
477 (3) Stockwell, B. R.; Friedmann Angeli, J. P.; Bayir, H.; Bush, A. L.;
478 Conrad, M.; Dixon, S. J.; Fulda, S.; Gascon, S.; Hatzios, S. K.; Kagan,
479 V. E.; Noel, K.; Jiang, X.; Linkermann, A.; Murphy, M. E.;
480 Overholtzer, M.; Oyagi, A.; Pagnussat, G. C.; Park, J.; Ran, Q.;
481 Rosenfeld, C. S.; Salnikow, K.; Tang, D.; Torti, F. M.; Torti, S. V.;
482 Toyokuni, S.; Woerpel, K.A.; Zhang, D. D. Ferroptosis: A Regulated
483 Cell Death Nexus Linking Metabolism, Redox Biology, and Disease.
484 *Cell* **2017**, *171*, 273–285.
485 (4) Yang, W. S.; SriRamaratnam, R.; Welsch, M. E.; Shimada, K.;
486 Skouta, R.; Viswanathan, V. S.; Cheah, J. H.; Clemons, P. A.; Shamji,
487 A. F.; Clish, C. B.; et al. Regulation of Ferroptotic Cancer Cell Death
488 by GPX4. *Cell* **2014**, *156*, 317–331.
489 (5) Larraufie, M.-H.; Yang, W. S.; Jiang, E.; Thomas, A. G.; Slusher,
490 B. S.; Stockwell, B. R. Incorporation of metabolically stable ketones
491 into a small molecule probe to increase potency and water solubility.
492 *Bioorg. Med. Chem. Lett.* **2015**, *25*, 4787–4792.

(6) Jiang, X.; Stockwell, B. R.; Conrad, M. Ferroptosis: mechanisms, 493
biology and role in disease. *Nat. Rev. Mol. Cell Biol.* **2021**, *22*, 266– 494
282. 495
(7) Weiland, A.; Wang, Y.; Wu, W.; Lan, X.; Han, X.; Li, Q.; Wang, 496
J. Ferroptosis and Its Role in Diverse Brain Diseases. *Molecular* 497
Neurobiology **2019**, *56*, 4880–4893. 498
(8) Friedmann Angeli, J. P.; Krysko, D. V.; Conrad, M. Ferroptosis 499
at the crossroads of cancer-acquired drug resistance and immune 500
evasion. *Nat. Rev. Cancer* **2019**, *19*, 405–414. 501
(9) Chen, X.; Kang, R.; Kroemer, G.; Tang, D. Broadening horizons: 502
the role of ferroptosis in cancer. *Nat. Rev. Clin Oncol.* **2021**, *18*, 280– 503
296. 504
(10) Feng, H.; Schorpp, K.; Jin, J.; Yozwiak, C. E.; Hoffstrom, B. G.; 505
Decker, A. M.; Rajbhandari, P.; Stokes, M. E.; Bender, H. G.; Csuka, J. 506
M.; et al. Transferrin Receptor Is a Specific Ferroptosis Marker. *Cell* 507
Rep. **2020**, *30*, 3411–3423. 508
(11) Cheng, Y.; Zak, O.; Aisen, P.; Harrison, S. C.; Walz, T. 509
Structure of the Human Transferrin Receptor-Transferrin Complex. 510
Cell **2004**, *116*, 565–576. 511
(12) Yang, W. S.; Stockwell, B. R. Synthetic lethal screening 512
identifies compounds activating iron-dependent, non-apoptotic cell 513
death in oncogenic-RAS-harboring cancer cells. *Chem. Biol.* **2008**, *15*, 514
234–245. 515
(13) Chen, X.; Gao, C.; Yan, Y.; Cheng, Z.; Chen, G.; Rui, T.; Luo, 516
C.; Gao, Y.; Wang, T.; Chen, X.; et al. Ruxolitinib exerts 517
neuroprotection via repressing ferroptosis in a mouse model of 518
traumatic brain injury. *Exp. Neurol.* **2021**, *342*, 113762. 519
(14) Fan, Z.; Cai, L.; Wang, S.; Wang, J.; Chen, B. Baicalin Prevents 520
Myocardial Ischemia/Reperfusion Injury Through Inhibiting ACSL4- 521
Mediated Ferroptosis. *Front Pharmacol.* **2021**, *12*, 628988. 522
(15) Sommer, C.; Gerlich, D. W. Machine learning in cell biology – 523
teaching computers to recognize phenotypes. *J. Cell Sci.* **2013**, *126*, 524
5529–5539. 525
(16) Bertrand, R.; Solary, E.; O'Connor, P.; Kohn, K. W.; Pommier, 526
Y. Induction of a Common Pathway of Apoptosis by Staurosporine. 527
Exp. Cell Res. **1994**, *211*, 314–321. 528
(17) Wyllie, A. H.; Kerr, J. F. R.; Currie, A. R. Cell Death: The 529
Significance of Apoptosis. *Int. Rev. Cytol.* **1980**, *68*, 251–306. 530
(18) Tibshirani, R. Regression shrinkage and selection via the lasso: 531
a retrospective. *J. R Stat Soc. Series B Stat Methodol.* **2011**, *73*, 273– 532
282. 533
(19) Friedman, J.; Hastie, T.; Tibshirani, R. Regularization Paths for 534
Generalized Linear Models via Coordinate Descent. *Journal of* 535
Statistical Software **2010**, *33*, 1–22. 536